ORIGINAL PAPER

Structural, Cation Distribution, and Magnetic Properties of CoFe$_2$O$_4$ Spinel Ferrite Nanoparticles Synthesized Using a Starch-Assisted Sol–Gel Auto-Combustion Method

**Raghvendra Singh Yadav · Jaromir Havlica · Jiri Masilko · Lukas Kalina ·
Miroslava Hajdúchová · Vojtěch Enev · Jaromir Wasserbauer · Ivo Kuřitka ·
Zuzana Kozakova**

Abstract In this article, cobalt ferrite nanoparticles were synthesized using a starch-assisted sol–gel auto-combustion route. The significant role played by further annealing temperatures of 300, 500, 700, 900 and 1100 °C on particle size and magnetic properties of ferrite nanoparticles was explored and reported. The prepared nanoparticles were characterized by X-ray diffraction (XRD), field emission scanning electron microscopy (FESEM), Raman spectroscopy, Fourier transform infrared spectroscopy, X-ray photoelectron spectroscopy and using a vibrating sample magnetometer. The X-ray diffraction patterns demonstrated single phase formation of CoFe$_2$O$_4$ spinel ferrite nanoparticles at different annealing temperatures. The FESEM analysis indicated a change of particle size and morphology at higher annealing temperature. The change in Raman modes and infrared absorption bands was observed with change of particle size and cation distribution. The highest value of coercivity (1091.2 Oe) and the saturation magnetization (54.76 erg g^{-1}) were obtained at annealing temperatures of 900 and 1100 °C, respectively. X-ray photoelectron spectroscopy revealed the presence of Co^{2+} and Fe^{3+} at octahedral and tetrahedral sites in CoFe$_2$O$_4$ nanoparticles. Further, the cation redistribution with change of particle size was confirmed by X-ray photoelectron spectroscopy.

R. S. Yadav (✉) · J. Havlica · J. Masilko · L. Kalina ·
M. Hajdúchová · V. Enev · J. Wasserbauer
Materials Research Centre, Brno University of Technology,
Purkyňova 464/118, 612 00 Brno, Czech Republic
e-mail: yadav@fch.vutbr.cz

I. Kuřitka · Z. Kozakova
Centre of Polymer Systems, University Institute, Tomas Bata
University in Zlín, Nad Ovčírnou 3685,
760 01 Zlín, Czech Republic

1 Introduction

Recently, spinel ferrite magnetic nanomaterials have attracted much attention because of their potential application in magnetic resonance imaging, drug delivery, magnetic fluids, spintronics, high density magnetic recording, catalysis, gas sensors, etc. [1]. Among the spinel ferrites, cobalt ferrite has been extensively studied because of its excellent chemical stability, mechanical hardness, high coercivity, reasonable saturation magnetization and high magnetocrystalline anisotropy [2, 3]. Its higher magnetocrystalline anisotropy compared to other spinel ferrites is due to the orbital angular momentum of Co^{2+} not being completely quenched by the crystalline field. Consequently, Co^{2+} on the octahedral sites of the crystal lattice contributes an orbital moment, comparable to the spin moment, resulting in strong spin–orbit coupling which is responsible for the characteristic properties of cobalt ferrite [4]. The bulk cobalt ferrite crystallizes in a partially inverse spinel structure (space group $Fd3m - O_h^7$) with the formula, $\left(Co_{1-\delta}^{+2}Fe_{\delta}^{+3}\right)\left[Co_{\delta}^{+2}Fe_{2-\delta}^{+3}\right]O_4$, where the round and square brackets denote tetrahedral (A) and octahedral (B) sites, respectively, and δ represents the degree of inversion; the fraction of the A sites is occupied by Fe^{3+} cations. If $\delta = 1$, the structure is called inverse spinel; if $\delta = 0$, the structure is called normal spinel; otherwise, it is called mixed spinel. The value of δ also depends on the thermal history of formation of cobalt ferrite [5].

The change in the exchange interaction between the tetrahedral and octahedral site cations in cobalt ferrite is

a key to controlling the magnetic properties. The magnetic properties of cobalt ferrite are also affected by particle size, morphology, composition, synthesis parameters and synthesis methods [6]. Until now, magnetic spinel ferrite nanoparticles have been synthesized by various synthesis methods, such as co-precipitation, sol–gel, micro-emulsion, combustion, hydrothermal method, etc. [7–16]. This article presents the effect of annealing temperature on the structural cation distribution and magnetic properties of $CoFe_2O_4$ nanoparticles. In this work, cobalt ferrite nanoparticles were synthesized using a starch-assisted sol–gel auto-combustion route and further annealed at the temperatures 300, 500, 700, 900 and 1100 °C to achieve different sized ferrite nanoparticles. Further, the change in magnetic properties with a change in particle size was observed. The change in cation redistribution with change of particle size was studied by X-ray photoelectron spectroscopy.

2 Experimental Section

2.1 Chemicals

Iron(III) nitrate nonahydrate ($Fe(NO_3)_3 \cdot 9H_2O$) and cobalt(II)nitrate hexahydrate ($Co(NO_3)_2 \cdot 6H_2O$) were purchased from Alfa Aesar GmbH & Co KG, Germany. Starch-soluble ($C_6H_{10}O_5)_n$ (from potatoes) was purchased from Lach-Ner, Czech Republic. In this study, the obtained chemicals were of analytical reagent grade and were used as received without any further purification.

2.2 Preparation of Ferrite Nanoparticles

Different sized $CoFe_2O_4$ nanoparticles were synthesized using a starch-assisted sol–gel auto-combustion method and by further annealing at different temperatures. The stoichiometric amount of cobalt nitrate ($Co(NO_3)_2 \cdot 6H_2O$) and iron nitrate ($Fe(NO_3)_3 \cdot 9H_2O$) was dissolved in distilled water to obtain a mixed solution. The reaction procedure was carried out in an air atmosphere. The molar ratio of cobalt nitrate to iron nitrate was 1:2. The metal nitrates were dissolved together in the minimum amount of double-distilled water needed to obtain a clear solution. An aqueous solution of starch ($C_6H_{10}O_5)_n$ (from potatoes) was mixed with the metal–nitrate solution. The mixed solution was placed on a hot plate with continuous stirring at 100 °C. During evaporation, the solution formed a very viscous brown gel. Then, the gel was heated to 200 °C to initiate a self-sustaining combustion reaction and produce as-burnt ferrite powder. Finally, the as-burnt powders were additionally annealed in a furnace in air atmosphere at 300, 500, 700, 900, and 1100 °C for 2 h.

2.3 Characterization

The structure and phase formation of cobalt ferrite nanoparticles annealed at different temperatures were characterized through a PANalytical Empyrean X-ray diffractometer with CuKα radiation (1.5406 Å). Fourier transform infrared (FTIR) spectra were recorded with a Nicolet iS 50 FTIR spectrometer using the ATR method. The morphology and size of $CoFe_2O_4$ ferrite nanoparticles were examined using a field emission gun scanning electron microscope (FEGSEM; JEOL Model JSM-7600F). Raman spectra were measured using a confocal microscope with a spectrometer ("Nanofinder-S"; SOLAR TII, Ltd.). Magnetic measurements of ferrite nanoparticles were performed using a vibrating sample magnetometer (VSM 7407; Lake Shore) at room temperature with maximum applied magnetic field of 10 kOe. Information about the presence of the element, its oxidation states, and cation distribution in nanoparticles was studied by X-ray photoelectron spectroscopy (XPS) using Kratos Analytical Axis Ultra DLD.

3 Result and Discussion

3.1 Crystal Structure

Figure 1 evidences the powder X-ray diffraction patterns of cobalt ferrite nanoparticles synthesized using the starch-assisted sol–gel auto-combustion method and annealed at 300, 500, 700, 900 and 1100 °C for 2 h. The X-ray diffraction (XRD) pattern showed the reflection planes of (220), (331), (222), (400), (422), (511) and (440), which confirm the presence of single-phase cubic spinel type lattice of $CoFe_2O_4$ (JCPDS file No. 22-1086) [17]. The XRD pattern of cobalt ferrite nanoparticles annealed at 300 °C shows very broad peaks, indicating ultra-fine nature and small crystallite size of the cobalt ferrite nanoparticles. The XRD patterns of the cobalt ferrite nanoparticles show an improvement in the sharpness and intensity of the crystallite peaks with increasing annealing temperature. The increase in crystallite size with annealing temperature was observed, as shown in Table 1. The observed increase in cobalt ferrite nanoparticles size with annealing temperature is most likely due to the fact that higher annealing temperature and time increase the coalescence process resulting in an increase in the particle size of cobalt ferrite nanoparticles [18]. The crystallite size of the cobalt ferrite nanoparticles is estimated from the full width at half maximum (FWHM) of the strongest diffraction peak using the Scherrer formula [19]

$$D = \kappa\lambda/\beta\cos\theta$$

where D k, β λ and θ are the crystallite size, the shape function, the FWHM of the (440) peak, the X-ray
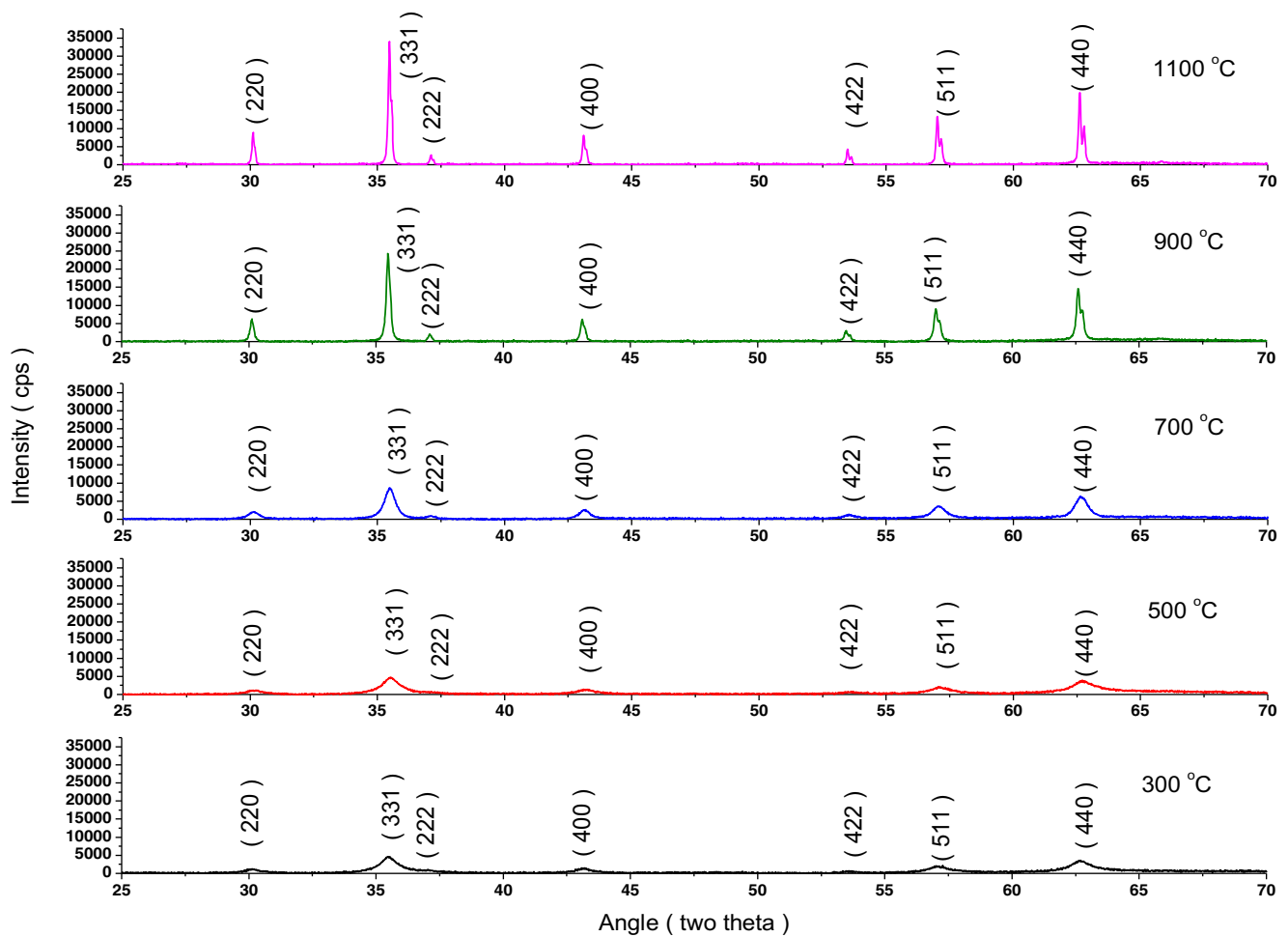
Fig. 1 X-ray diffraction pattern of CoFe$_2$O$_4$ nanoparticles synthesized using the starch-assisted sol–gel auto-combustion method and annealed at 300, 500, 700, 900 and 1100 °C for 2 h

wavelength and the diffraction angle, respectively. It is observed that with the increase of annealing temperature, the average crystallite size of cobalt ferrite nanoparticles increases in the following order: 7.14 nm (300 °C), 7.19 nm (500 °C), 13.96 nm (700 °C), 95.77 nm (900 °C), and 676.30 nm (1100 °C), as listed in Table 1.

3.2 Morphology and Particle Size Study

Figure 2 shows the field emission scanning electron microscopy (FESEM) image of cobalt ferrite nanoparticles annealed at 300 and 500 °C. The cobalt ferrite nanoparticles annealed at a lower annealing temperature were spherical and in the size range of 5–15 and 10–25 nm at 300 and

Table 1 Crystallite size (nm), M_s (emu/g), M_r (emu/g), H_c (Oe), K (erg/g), η_B (μ_B), and M_r / M_s value of CoFe$_2$O$_4$ nanoparticles synthesized using the starch-assisted sol–gel auto-combustion method and annealed at 300, 500, 700, 900 and 1100 °C

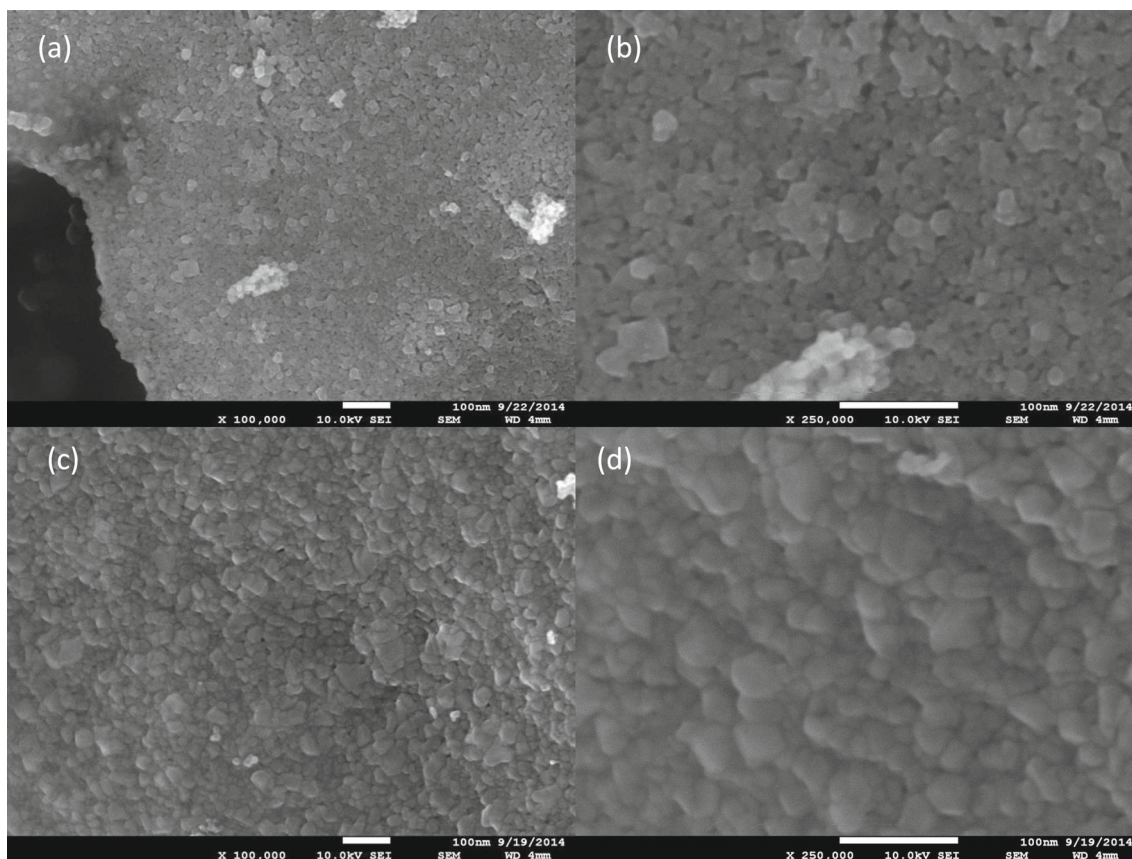| Annealing temperature (°C)	Crystallite size (nm)	M_s (emu/g)	M_r (emu/g)	H_c (Oe)	$K \times 10^3$ (erg/g)	η_B (μ_B)	M_r / M_s
300	7.14	23.92	4.8	285.44	7.11	1.00	0.20
500	7.19	26.42	5.7	387.84	10.67	1.11	0.22
700	13.96	36.77	12.5	736.99	27.10	1.54	0.34
900	95.77	52.55	22.1	1091.2	52.34	2.21	0.42
1100	676.30 (bulk)	54.76	17.5	540.72	30.84	2.30	0.32

Fig. 2 FESEM image of CoFe$_2$O$_4$ nanoparticles annealed at 300 °C (**a**, **b**) and 500 °C (**c**, **d**)

500 °C, respectively. The FESEM image indicated the increase in particle size with an increase of annealing temperature. Figure 3 shows the FESEM image of cobalt ferrite nanoparticles annealed at 700, 900, and 1100 °C. Some moderately agglomerated and some separated spherical ferrite particles were observed at 700 °C. Further, spherical and elongated bigger particles were observed at higher annealing temperatures. The cobalt ferrite nanoparticles annealed at higher annealing temperatures were in the size range of 20–40, 50–150, and 100–800 nm at 700, 900, and 1100 °C, respectively. The particle size derived from FESEM micrographs is found to be larger than that estimated from XRD data. This indicates that every spinel cobalt ferrite particle is formed by the aggregation of a large number of crystallites.

3.3 Raman Spectroscopy

Figure 4 shows the Raman spectrum of CoFe$_2$O$_4$ nanoparticles synthesized using the starch-assisted sol–gel auto-combustion method and annealed at different temperatures. CoFe$_2$O$_4$ nanoparticles annealed at 300 °C show six peak maxima at 190.2, 288.0, 460.0, 550.7, 602.8 and 673.2 cm^{-1}, as mentioned in Table 2, and most of which are the typical Raman modes of the cubic inverse spinel ferrite

structure. However, CoFe$_2$O$_4$ nanoparticles annealed at 500 °C show six peak maxima at 188.4, 289.8, 460.9, 559.2, 603.7 and 672.3 cm^{-1}. CoFe$_2$O$_4$ has a cubic inverse ferrite structure with O$_h^7$ (*Fd3m* space group) which gives rise to 39 normal vibrational modes, and out of which five are Raman active, namely A_{1g}, E_g and three T_{2g} [20]. Frequencies above 600 cm^{-1} are due to A_{1g} symmetry involving symmetric stretching of an oxygen atom with respect to a metal ion in tetrahedral voids. The other low frequency phonon modes are due to a metal ion involved in octahedral void, i.e., E_g and T_{2g}(3) [20]. These modes correspond to the symmetric and antisymmetric bending of oxygen atom in M–O bond at octahedral voids [21]. The change in Raman modes is also observed at higher annealing temperatures of 700, 900 and 1100 °C. CoFe$_2$O$_4$ nanoparticles annealed at 700 °C show six peak maxima at 185.7, 290.7, 461.6, 559.6, 604.6 and 671.6 cm^{-1}. Ferrite nanoparticles annealed at 900 °C show six peak maxima at 199.8, 300.4, 462.5, 567.5, 605.5 and 685.6 cm^{-1}. However, CoFe$_2$O$_4$ nanoparticles annealed at 1100 °C show six peak maxima at 205.2, 302.2, 464.3, 572.0, 607.1 and 690.1 cm^{-1}, as shown in Table 2. The variation in Raman modes of CoFe$_2$O$_4$ samples annealed at different temperatures is due to change of crystallite size and cation distribution [22, 23].
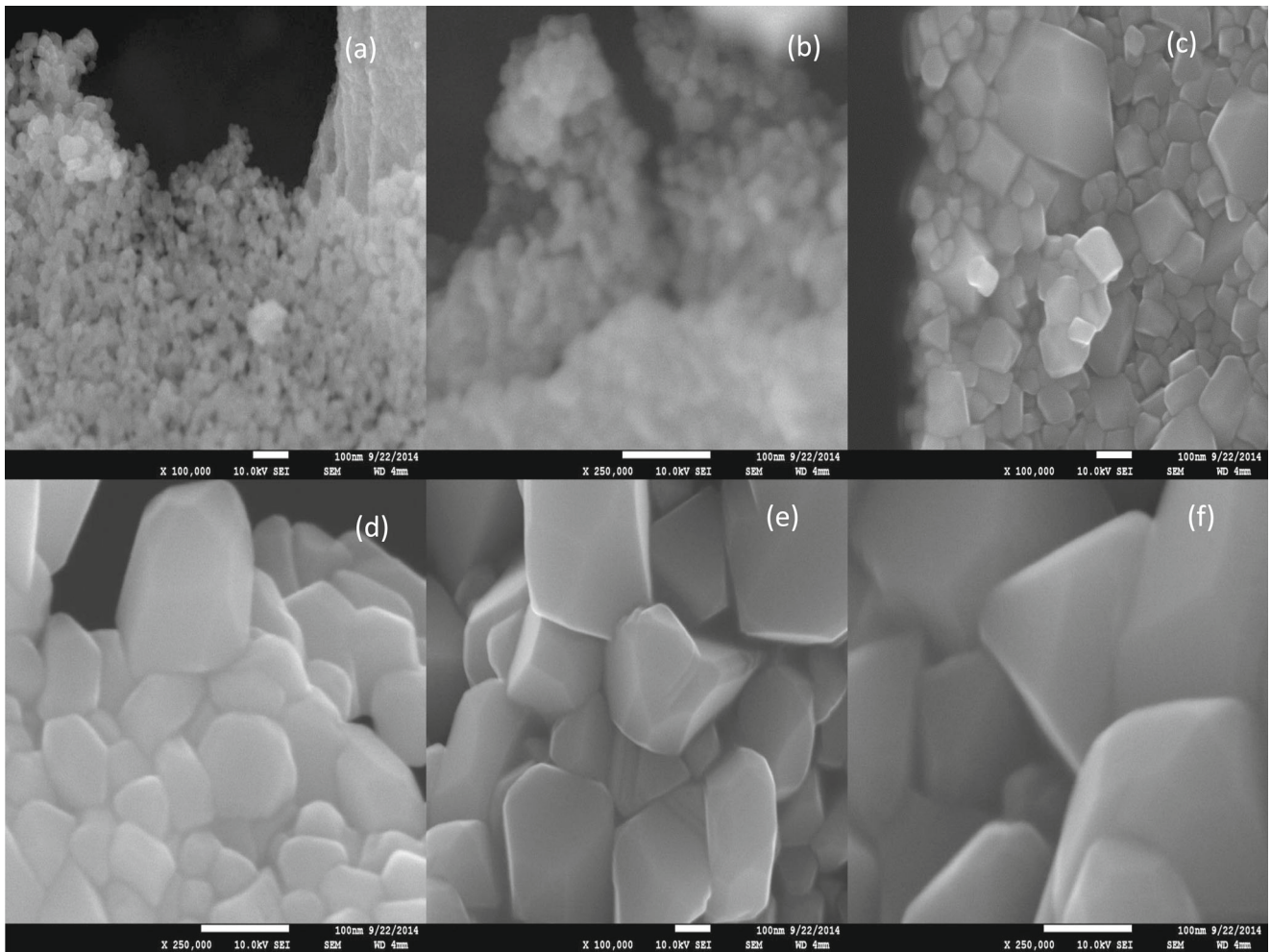
Fig. 3 FESEM image of CoFe$_2$O$_4$ nanoparticles annealed at 700 °C (**a**, **b**), 900 °C (**c**, **d**) and 1100 °C (**e**, **f**)

Fig. 4 Raman spectra of CoFe$_2$O$_4$ nanoparticles synthesized using the starch-assisted sol–gel auto-combustion method and annealed at 300, 500, 700, 900 and 1100 °C

Table 2 Raman modes of CoFe$_2$O$_4$ nanoparticles synthesized using the starch-assisted sol–gel auto-combustion method and annealed at 300, 500, 700, 900 and 1100 °C

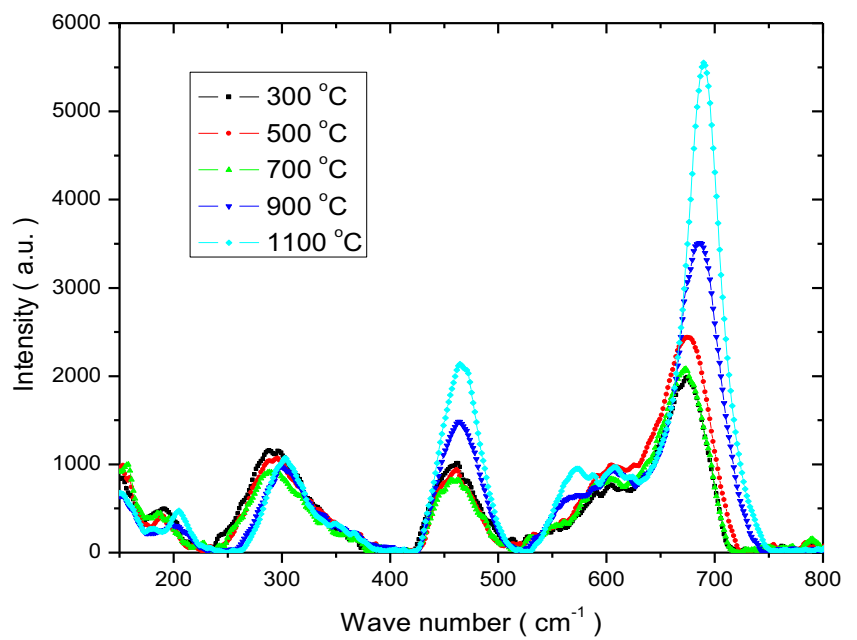| Annealing temperature (°C)	Raman peak (cm^{-1})					
	$A_{1g}(1)$	$A_{1g}(2)$	$T_{1g}(1)$	$T_{1g}(2)$	E_g	$T_{1g}(3)$
300	673.2	602.8	550.7	460.0	288.0	190.2
500	672.3	603.7	559.2	460.9	289.8	188.4
700	671.6	604.6	559.6	461.6	290.7	185.7
900	685.6	605.5	567.5	462.5	300.4	199.8
1100	690.1	607.1	572.0	464.3	302.2	205.2

3.4 Fourier Transform Infrared Spectroscopy

It can be observed from Fig. 5 that the FTIR spectra of all the samples show two principle absorption bands near 540 cm^{-1} (ν_1) and the second absorption band near 325 cm^{-1} (ν_2) [24, 25]. The difference in frequency between the characteristic vibrations ν_1 and ν_2 may be attributed to the changes in bond length of oxygen O^{2-} and metal ions Fe^{3+} at octahedral and tetrahedral sites. In the present study, the ν_1 frequency was 549.2, 544.11, 543.21, 524.24, and 519.12 cm^{-1} for CoFe$_2$O$_4$ nanoparticles prepared at 300, 500, 700, 900, and 1100 °C, respectively, as listed in Table 3. The ν_2 frequency was 342.4, 334.86, 326.73, 302.64, and 301.44 cm^{-1} for CoFe$_2$O$_4$ nanoparticles prepared at 300,
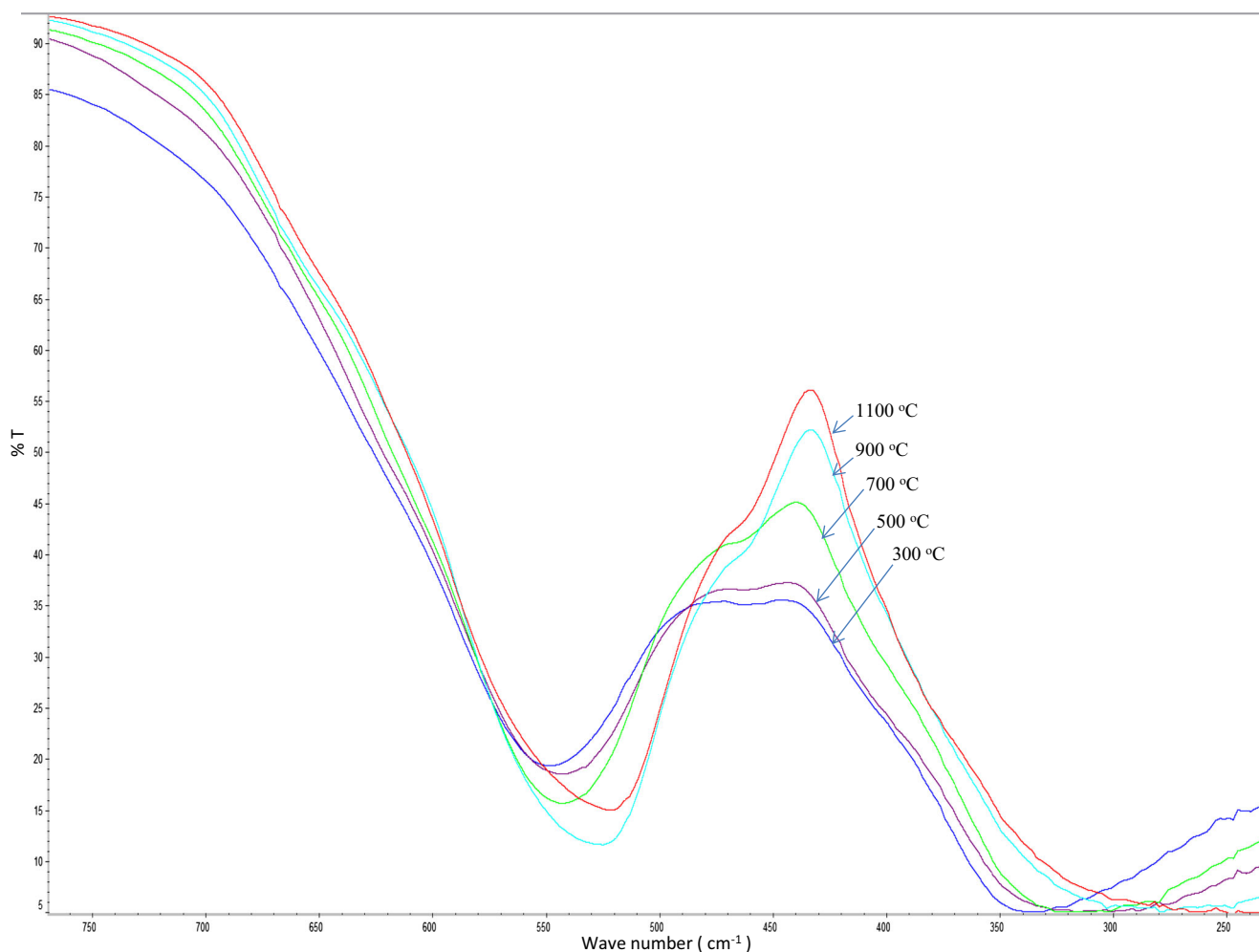

Fig. 5 FTIR spectra of CoFe$_2$O$_4$ nanoparticles synthesized using the starch-assisted sol–gel auto-combustion method and annealed at 300, 500, 700, 900 and 1100 °C

Table 3 Frequency (ν_1 and ν_2) and force constant (F_T and F_B) for the A and B sites, respectively;or CoFe$_2$O$_4$ nanoparticles synthesized using the starch-assisted sol–gel auto-combustion method and annealed at 300, 500, 700, 900 and 1100 °C

Annealing temperature (°C)	ν_1 (cm^{-1})	ν_2 (cm^{-1})	$F_T \times 10^5$ (dyne/cm^2)	$F_B \times 10^5$ (dyne/cm^2)
300	549.2	342.4	2.19	0.853
500	544.11	334.86	2.16	0.816
700	543.21	326.73	2.14	0.777
900	524.24	302.64	2.00	0.667
1100	519.12	301.44	1.96	0.661

500, 700, 900, and 1100 °C, respectively. The observed change in the absorption bands with annealing temperature is due to change of crystallite size and redistribution of Co^{2+} and Fe^{3+} ions at octahedral and tetrahedral sites in CoFe$_2$O$_4$ nanoparticles The broadening in ferrites has been commonly observed in the spectral bands. The broadening is due to the statistical distribution of cations over octahedral and tetrahedral sites [26]. It is well known that the vibration frequency is proportional to force constant (F); therefore, the band shift of ν_1 and ν_2 frequency with change of annealing temperature indicates that the force constant changes. The calculated values of the force constant F_T and F_B for the A and B sites, respectively, are listed in Table 3 using the following relation [27]:

$$F = 4\Pi^2 c^2 \nu^2 m$$

where F is the force constant, c is the light velocity 2.99 $\times$ 10^{10} cm s^{-1}, ν is the vibration frequency of the A and B sites, and m is the reduced mass for the Fe^{3+} ions and the O^{2-} ions ($\sim$ 2.065 $\times$ 10^{-23} g mol^{-1}). The value of force constant F_T ($\times$ 10^5 dyne/cm^2) was 2.19, 2.16, 2.14, 2.00 and 1.96 for CoFe$_2$O$_4$ nanoparticles annealed at 300, 500, 700, 900 and 1100 °C, respectively. However, the value

of force constant F_B ($\times$ 10^5 dyne/cm^2) was 0.853, 0.816, 0.777, 0.667 and 0.661 for CoFe$_2$O$_4$ nanoparticles annealed at 300, 500, 700, 900 and 1100 °C, respectively.

3.5 XPS Study

The XPS spectra of CoFe$_2$O$_4$ nanoparticles annealed at 500 and 900 °C were collected using high-resolution 2p regions of cobalt as shown in Figs. 6 and 7, respectively. High-resolution XPS spectra of Co show satellite peaks that appear on the high-binding energy side of both 2p$_{3/2}$ and 2p$_{1/2}$ regions for CoFe$_2$O$_4$ nanoparticles annealed at 500 and 900 °C. This observation of the strong satellite peak indicates that Co is in an oxidation state of +2. Satellite peaks appear due to the multiplet splitting for Co in the +2 state [28]. The Co region was further deconvoluted for the octahedral versus tetrahedral peaks and quantitative analyses. Further analysis of 2p$_{3/2}$ Co regions of the CoFe$_2$O$_4$ nanoparticles annealed at 500 and 900 °C shows obvious similarity in the 2p$_{3/2}$ peak shapes. Deconvolution of the 2p peak regions of both samples reveals the presence of two nonequivalent bonds due to two types of lattice sites, i.e., tetrahedral and octahedral. The binding energies
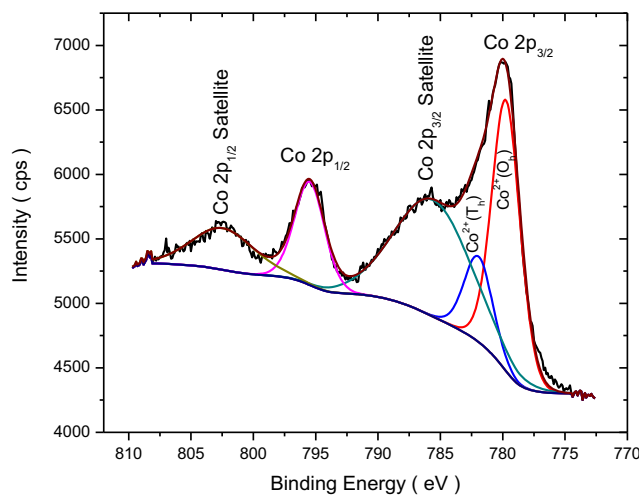

Fig. 6 Deconvolution of the Co 2p$_{3/2}$ region for CoFe$_2$O$_4$ nanoparticles annealed at 500 °C
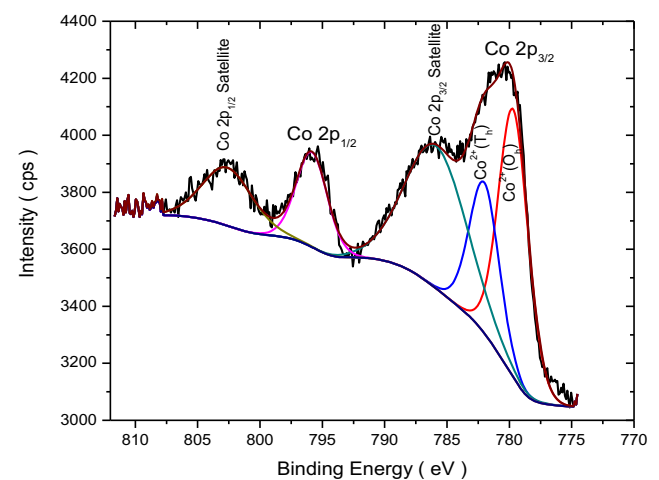
Fig. 7 Deconvolution of the Co 2p$_{3/2}$ region for CoFe$_2$O$_4$ nanoparticles annealed at 900 °C

associated with Co $2p_{3/2}$ for $CoFe_2O_4$ nanoparticles annealed at 500 °C is 779.7 and 781.9 eV. The binding energies associated with Co $2p_{3/2}$ for $CoFe_2O_4$ nanoparticles annealed at 900 °C is 779.6 and 782.0 eV. The binding energy peak 779.7 or 779.6 eV appears since Co^{2+} has octahedral (O_h) bonding with oxygen, whereas peak 781.9 or 782.0 eV is due to the tetrahedral (T_d) bonding of Co^{2+} with oxygen. For $CoFe_2O_4$ nanoparticles annealed at 500 °C, the relative contributions to the overall intensity of Co^{2+} ions at the octahedral and tetrahedral sites were 76 and 24 %, respectively. However, for $CoFe_2O_4$ nanoparticles annealed at 900 °C, the relative contributions to the overall intensity of Co^{2+} ions at the octahedral and tetrahedral sites were 64 and 36 %, respectively, as shown in Table 4.

Figures 8 and 9 show the Fe 2p core electron spectrum for $CoFe_2O_4$ nanoparticles annealed at 500 and 900 °C, respectively. To confirm the presence of Fe^{3+} in the $CoFe_2O_4$ nanoparticles annealed at 500 and 900 °C, the Fe 2p XPS spectra were fitted using Gaussian–Lorentzian (GL30) line shapes after subtracting a Shirley-type background, as shown in Figs. 8 and 9. Based on spin–orbit splitting, it consists of Fe $2p_{3/2}$ and Fe $2p_{1/2}$ components. An additional peak exists as a satellite peak in between Fe $2p_{1/2}$ and Fe $2p_{3/2}$. The satellite peak was at 718.5 eV for $CoFe_2O_4$ nanoparticles annealed at 500 °C and at 719.1 eV for $CoFe_2O_4$ nanoparticles annealed at 900 °C. The difference between 6.0 eV for $CoFe_2O_4$ nanoparticles annealed at 500 °C and 6.2 eV for $CoFe_2O_4$ nanoparticles annealed at 900 °C from the satellite peak to Fe $2p_{1/2}$ peak is identified as Fe^{3+} state in the both samples [29]. The shape of XPS peak for these two samples is similar and asymmetric. It indicates the presence of two nonequivalent bonds of Fe ions in $CoFe_2O_4$ spinel ferrite nanoparticles, which are consistent with that there are two kinds of lattice sites for Fe ion occupancy in $CoFe_2O_4$ spinel ferrite nanoparticles. Deconvolution of the 2p peak regions of both samples reveals the presence of tetrahedral and octahedral sites. For $CoFe_2O_4$ nanoparticles annealed at 500 °C, it yields Fe $2p_{3/2}$ binding energies of 710.1 and 712.4 eV. For $CoFe_2O_4$ nanoparticles annealed at 900 °C, it yields Fe $2p_{3/2}$ binding energies of
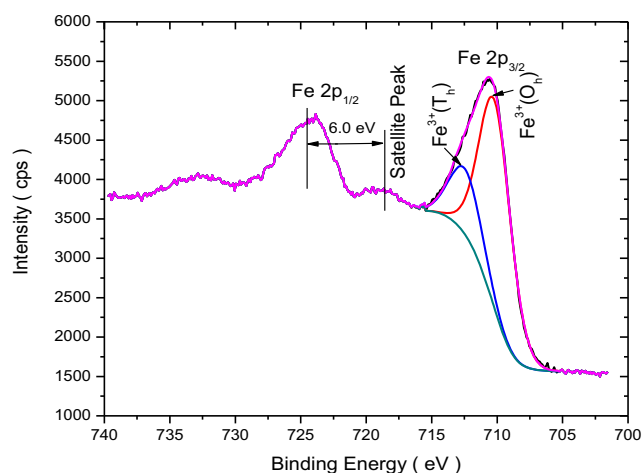

Fig. 8 Deconvolution of the Fe $2p_{3/2}$ region for $CoFe_2O_4$ nanoparticles annealed at 500 °C

710.2 and 712.5 eV. The doublets in $CoFe_2O_4$ nanoparticles annealed at 500 and 900 °C can be ascribed to Fe^{3+} ions in octahedral and tetrahedral sites, respectively. The relative contributions to the overall intensity of Fe^{3+} ions at octahedral and tetrahedral sites are 76 and 24 % for $CoFe_2O_4$ nanoparticles annealed at 500 °C. However, the relative contributions to the overall intensity of Fe^{3+} ions at octahedral and tetrahedral sites are 67 and 33 % for $CoFe_2O_4$ nanoparticles annealed at 900 °C. From the XPS data, the occupation formula for the $CoFe_2O_4$ nanoparticles annealed at 500 and 900 °C is $\left(Co_{0.24}^{+2}Fe_{0.48}^{+3}\right)\left[Co_{0.76}^{+2}Fe_{1.52}^{+3}\right]O_4$ and $\left(Co_{0.36}^{+2}Fe_{0.66}^{+3}\right)\left[Co_{0.64}^{+2}Fe_{1.34}^{+3}\right]O_4$, respectively. Where brackets ( ) and [ ] denote tetrahedral and octahedral sites, respectively [30].

3.6 Magnetic Property

Magnetic hysteresis loops of the cobalt ferrite nanoparticles synthesized using the starch-assisted sol–gel autocombustion method and annealed at 300, 500, 700, 900 and 1100 °C are shown in Fig. 10. Magnetic measurements show

Table 4 The analysis result of Co 2p and Fe 2p XPS spectra for the $CoFe_2O_4$ nanoparticles annealed at 500 and 900 °C

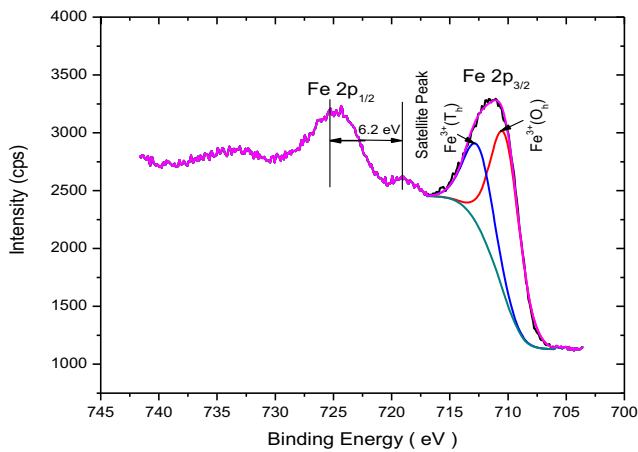| Sample	Spectrum	B.E. (eV)	Assignment	Atomic percentage (%)
$CoFe_2O_4$ annealed at 500 °C	Co $2p_{3/2}$	779.7	Octahedral Co^{2+}	76
		781.9	Tetrahedral Co^{2+}	24
	Fe $2p_{3/2}$	710.1	Octahedral Fe^{3+}	76
		712.4	Tetrahedral Fe^{3+}	24
$CoFe_2O_4$ annealed at 900 °C	Co $2p_{3/2}$	779.6	Octahedral Co^{2+}	64
		782.0	Tetrahedral Co^{2+}	36
	Fe $2p_{3/2}$	710.2	Octahedral Fe^{3+}	67
		712.5	Tetrahedral Fe^{3+}	33

Fig. 9 Deconvolution of the Fe $2p_{3/2}$ region for $CoFe_2O_4$ nanoparticles annealed at 900 °C

that all of the nanoparticles exhibit a ferrimagnetic behavior. The magnetic parameters such as the saturation magnetization values (M_s), remanent magnetization (M_r) values, and coercivity (H_c) values of the cobalt ferrite nanoparticles were calculated from the hysteresis curve shown in Fig. 10 and are shown in Table 1. An important characteristic observed in the hysteresis loops was the change in saturation magnetization (M_s) in the $CoFe_2O_4$ nanoparticles at different annealing temperatures. The largest saturation magnetization value was found to be 54.76 emu g^{-1} for cobalt ferrite nanoparticles annealed at 1100 °C. However, the smallest value was found to be 23.92 emu g^{-1} for cobalt ferrite nanoparticles annealed at 300 °C. The saturation magnetization for the smaller size cobalt ferrite nanoparticles is found to be lower than that for higher-size cobalt ferrite nanoparticles, which can be attributed to

surface spin canting. The increase of saturation magnetization with increase in annealing temperature is an indication that the average magnetic domain size of the particles is increasing and the atomic spins are getting more and more aligned with the direction of the applied magnetic field. The increase in coercivity from 285.44 Oe (at 300 °C) to 1091.20 Oe (at 900 °C) with an increase of annealing temperature was found. However, a decrease in coercivity from 1091.20 Oe (at 900 °C) to 542.72 Oe (at 1100 °C) with further increase of annealing temperature was found. Therefore, the coercivity value was increased until it reached a maximum value and then began to diminish. In other words, the larger value of coercivity at lower annealing temperature is due to single domain cobalt ferrite nanoparticles, which then decreases on further annealing due to the formation of multi-domains after single-domain size limit of the cobalt ferrite nanoparticles. However, in the magnetic properties of ferrite nanoparticles, there is an interplay of four factors, namely superexchange interaction, magnetocrystalline anisotropy, canting effect, and dipolar interactions between the projected moments on the surface [31]. Prabhakaran and Hemalatha [32] reported the magnetization behavior of ferrite nanoparticles on the basis of changes in an exchange interaction between tetrahedral and octahedral sub-lattices. Peddis et al. [33] explained the effect of magnetic disorder on saturation magnetization by the interplay between spin canting and inversion degree. $CoFe_2O_4$ has an inverse spinel structure in which Co^{2+} occupies the octahedral site and Fe^{3+} ions equally occupied tetrahedral and octahedral sites, with their spins in the opposite direction. In $CoFe_2O_4$, the magnetic properties primarily depend on the Co^{2+} ions. The distribution of cations between A and B sites depend on the preparation method, the type of bonding, and ionic radius.

Fig. 10 The magnetic hysteresis loop of $CoFe_2O_4$ nanoparticles synthesized using the starch-assisted sol–gel auto-combustion method and annealed at 300, 500, 700, 900 and 1100 °C
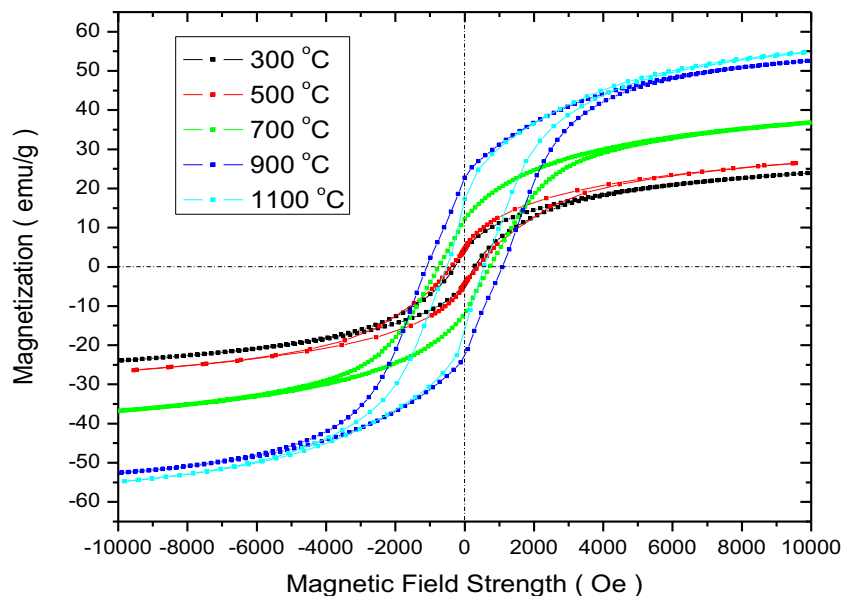
The magnetic moment per formula unit, according to Neel's two sub-lattice model, is given by the difference of magnetic moment of each sub-lattice [34].

$$M = M_A - M_B$$

In the above equation, M_A and M_B are the A and B sub-lattice magnetic moments in μ_B, respectively. According to Neel's postulate [34], magnetic moments of ferrites are a sum of magnetic moments of individual sub-lattices. Exchange interaction between electrons of ions in these sub-lattices has different values. Generally, an interaction between magnetic ions of sub-lattices "A" and "B" (A–B interaction) is the strongest. The A–A interaction is almost ten times weaker, and B–B interaction is the weakest. The dominant A–B interaction leads to complete or partial (non-compensated) ferrimagnetism [34]. Recently, Ghatreh-Samani et al. [35] mentioned that by increasing the annealing temperature of the $MnFe_2O_4$ nanoparticles, Fe^{3+} ions transferred from B site to A site, and therefore, the accumulation of Fe^{3+} ions increased in A site; consequently, the $Fe_A^{3+} - F_B^{3+}$ superexchange interactions increased and this led to an increase in saturation magnetization. Li et al. [36] also reported the increase of saturation magnetization in $MnFe_2O_4$ nanoparticles with an increase of annealing temperature. This research group observed that when the calcination temperature increases from 450 to 700 °C, the occupation ratio of Fe^{3+} ions at the octahedral sites decreases from 42.5 to 38.9 % and this led to an increase in the net magnetic moment. In this present study, XPS study support the transfer of higher magnetic moment Fe^{3+} ions (5 μ_B) as well as lower magnetic moment Co^{2+} (3 μ_B) from B site to A site in $CoFe_2O_4$ nanoparticles with an increase of annealing temperature, as listed in Table 4. Therefore, the increase in saturation magnetization with an annealing temperature of cobalt ferrite nanoparticles is due to an increase of the A–B superexchange interactions.

The decrease of magneton number (η_B) from 2.30 to 1.0 μ_B was observed in $CoFe_2O_4$ nanoparticles with a decrease in annealing temperature, as shown in Table 1. Decrease in magneton number (μ_B) (the saturation magnetization per formula unit in μ_B) is associated with the decrease in A–B interaction, and it is calculated using the relation [37–39]:

$$\eta_B = (\text{mol weight} \times M_s)/5585$$

The dependence of anisotropy constant (K) on the annealing temperature, as listed in Table 1, is evaluated by using the relation [40, 41]:

$$H_c = 0.96 K/M_s$$

where K is an anisotropy constant.

The increase in anisotropy constant from 7.11×10^3 erg g^{-1} (at 300 °C) to 52.34×10^3 erg g^{-1} (at 900 °C) with an increase of annealing temperature was found. However,

with further increase of annealing temperature, a decrease in anisotropy constant from 52.34×10^3 erg g^{-1} (at 900 °C) to 30.84×10^3 erg g^{-1} (at 1100 °C) was observed. Therefore, magnetocrystalline anisotropy is affected by cationic redistribution and change in magnetic domain regime due to reduction in the average crystalline size [42].

4 Conclusion

In this work, we demonstrated magnetic properties of cobalt ferrite nanoparticles dependent on particle size and cation distribution on octahedral and tetrahedral sites. These cobalt ferrite nanoparticles were synthesized using the starch-assisted sol–gel auto-combustion route and further annealed at the temperatures 300, 500 700, 900 and 1100 °C to achieve different particle sizes of ferrite. The X-ray diffraction patterns demonstrated single phase formation of $CoFe_2O_4$ spinel ferrite nanoparticles. The FESEM analysis indicated a change of particle size and morphology at higher annealing temperature. The Raman spectroscopy and Fourier transform infrared (FTIR) spectroscopy supported the formation of ferrite phase and change in spectra with change of annealing temperature. Further, the cation redistribution with change of particle size was confirmed by X-ray photoelectron spectroscopy. X-ray photoelectron spectroscopy also confirmed the presence of Co^{2+} and Fe^{3+} at octahedral and tetrahedral sites in $CoFe_2O_4$ nanoparticles. From the XPS analysis, the occupation formula for the $CoFe_2O_4$ nanoparticles annealed at 500 and 900 °C was $\left(Co_{0.24}^{+2}Fe_{0.48}^{+3}\right)\left[Co_{0.76}^{+2}Fe_{1.52}^{+3}\right]O_4$ and $\left(Co_{0.36}^{+2}Fe_{0.66}^{+3}\right)\left[Co_{0.64}^{+2}Fe_{1.34}^{+3}\right]O_4$, respectively. The highest value of coercivity (1091.2 Oe) and saturation magnetization (54.76 erg g^{-1}) were obtained at annealing temperatures 900 and 1100 °C, respectively.

References

1. Mohammed, E.M., Malini, K.A., Joy, P.A., Kulkarni, S.D., Date, S.K., Kurian, P., Anantharaman, M.R.: Plast. Rubber Compos. **31**, 106 (2002)
2. Sugimoto, M.: J. Am. Ceram. Soc. **82**(2), 269 (1999)
3. Liu, Y.-L., Liu, Z.-M., Yang, Y., Yang, H.-F., Shen, G.-L., Yu, R.-Q.: Sens. Actuators **B107**, 600 (2005)
4. Nlebedim, I.C., Melikhov, Y., Jiles, D.C.: J. Appl. Phys. **115**, 043903 (2014)
5. Junior, A.F., e Silva, F.C.: Appl. Phys. Lett. **96**, 172505 (2010)
6. Kim, Y.I., Kim, D., Lee, C.S.: Physica B **337**, 42 (2003)

7. Huang, X.-H., Chen, Z.-H.: Scr. Mater. **54**, 169 (2006)
8. Choi, E.J., Ahu, Y., Kim, S., Hyun An, D.: J. Magn. Magn. Mater. **262**, L198 (2003)
9. Junior, A.F., Lima, E.C.O.: J. Magn. Magn. Mater. **308**, 198 (2007)
10. Hutlova, A., Niznansky, D., Rehspringer, J.-L., Estournes, C., Kurmoo, M.: Adv. Mater. **15**, 1622 (2003)
11. Pillai, V., Shah, D.O.: J. Magn. Magn. Mater. **163**, 243 (1996)
12. Shafi, K.V.P.M., Gedanken, A., Prozorov, R., Balogh, J.: Chem. Mater. **10**, 3445 (1998)
13. Kim, Y.I., Kim, D., Lee, C.S.: Physica B **337**, 42 (2003)
14. Mumtaz, A., Maaz, K., Janjua, B., Hasanain, S.K., Bertino, M.F.: J. Magn. Magn. Mater. **313**, 266 (2007)
15. Seip, C.T., Carpenter, E.E., O'Connor, C.J., John, V.T., Li, S.: IEEE Trans. Magn. **34**, 1111 (1998)
16. Cote, L.J., Teja, A.S., Wilkinson, A.P., Zhang, Z.J.: Fluid Phase Equilibr. **210**, 307 (2003)
17. Briceno, S., Bramer-Escamilla, W., Silva, P., Delgado, G.E., Plaza, E., Palacios, J., Canizales, E.: J. Magn. Magn. Mater. **324**, 2926 (2012)
18. Maaz, K., Karim, S., Mumtaz, A., Hasanain, S.K., Liu, J., Duan, J.L.: J. Magn. Magn. Mater. **321**, 1838 (2009)
19. Cullity, B.D.: Addison-Wesley, vol. 102, pp. 1978
20. Chandramohan, P., Srinivasan, M.P., Velmurugan, S., Narasimhan, S.V.: J. Solid State Chem. **184**, 89 (2011)
21. Wang, Z., Lazor, P., Saxena, S.K., O'Neill, H.S.C.: Mater. Res. Bull. **37**, 1589 (2002)
22. Gabriel, S., Einat, T., Tsachi, L., Markovich, G.: J. Phys. Chem. C **111**, 14334 (2007)
23. Liu, W., Chan, Y., Cai, J., Leung, C., Mak, C., Wong, K., Zhang, F., Wu, X., Qi, X.D.: J. Appl. Phys. **112**, 104306 (2012)
24. Waldron, R.D.: Phys. Rev. **99**, 1727 (1955)
25. Raut, A.V., Barkule, R.S., Shengule, D.R., Jadhav, K.M.: J. Magn. Magn. Mater. **87**, 358–359 (2014)
26. Srinivasan, T.T., Srivastava, C.M., Venkatramni, N., Patani, M.J.: Bull. Mater. Sci. **5**, 1063 (1984)
27. Zaki, H.M., Dawoud, H.A.: Physica B **405**, 4476 (2010)
28. Jaffari, G.H., Lin, Y., Ni, C., Shah, S.I.: Mater. Sci. Eng. B **164**, 23 (2009)
29. Tholkappiyan, R., Vishista, K.: Physica B (2014). doi:10.1016/j.physb.2014.04.022
30. Zhou, Z., Zhang, Y., Wang, Z., Wei, W., Tang, W., Shi, J., Xiong, R.: Appl. Surf. Sci. **254**, 6972 (2008)
31. Prabhakaran, T., Hemalatha, J.: J. Alloys Compd. **509**, 7071 (2011)
32. Prabhakaran, T., Hemalatha, J.: Ceram. Int. **40**, 3315 (2014)
33. Peddis, D., Yaacoub, N., Ferretti, M., Martinelli, A., Piccaluga, G., Musinu, A., Cannas, C., Navarra, G., Greneche, J.M., Fiorani, D.: Phys. J.Condens. Matter **23**(426004), 8 (2011)
34. Neel, L.: Ann. Phys. Paris **3**, 137 (1948)
35. Ghatreh-Samani, R., Mostafaei, A.: J. Magn. Magn. Mater. doi:10.1016/j.jmmm.2014.11.005
36. Li, J., Yuan, H., Li, G., Liu, Y., Jinsong, L., Magn, J.: Magn. Mater. **322**, 3396 (2010)
37. Gadkari, A.B., Shinde, T.J., Vasambekar, P.N.: J. Magn. Magn. Mater. **322**, 3823 (2010)
38. Raut, A.V., Barkule, R.S., Shengule, D.R., Jadhav, K.M.: J. Magn. Magn. Mater. **358–359**, 87 (2014)
39. Yadav, R.S., Havlica, J., Kuřitka, I., Kozakova, Z., Masilko, J., Hajdúchová, M., Enev, V., Wasserbauer, J.: J. Supercond. Nov. Magn. doi:10.1007/s10948-014-2849-9
40. Yadav, R.S., Havlica, J., Ptáček, P., Kuřitka, I., Kožáková, Z., Palou, M., Bartoníčková, E., Boháč, M., Frajkorová, F., Masilko, J., Zmrzlý, M., Hajdúchová, M., Enev, V.: J. Supercond. Nov. Magn. doi:10.1007/s10948-014-2854-z
41. Yadav, R.S., Havlica, J., Ptáček, P., Kuřitka, I., Kožáková, Z., Palou, M., Bartoníčková, E., Boháč, M., Frajkorová, F., Masilko, J., Hajdúchová, M., Enev, V., Wasserbauer, J.: J. Supercond. Nov. Magn. doi:10.1007/s10948-014-2870-z
42. Yadav, R.S., Havlica, J., Hnatko, M., Šajgalík, P., Alexander, C., Palou, M., Bartoníčková, E., Boháč, M., Frajkorová, F., Masilko, J., Zmrzlý, M., Kalina, L., Hajdúchová, M., Enev, V.: J. Magn. Magn. Mater. **378**, 190 (2015)